



## MnO<sub>2</sub>/carbon nanowalls composite electrode for supercapacitor application

Sameh Hassan <sup>a</sup>, Masaaki Suzuki <sup>b</sup>, Shinsuke Mori <sup>b</sup>, Ahmed Abd El-Moneim <sup>a,\*</sup>

<sup>a</sup> Material Science and Engineering Department, Egypt–Japan University of Science and Technology, New Borg El Arab, Alexandria 21934, Egypt

<sup>b</sup> Department of Chemical Engineering, Tokyo Institute of Technology, 2-12-1 O-okayama, Meguro-ku, Tokyo 152-8552, Japan



### HIGHLIGHTS

- MnO<sub>2</sub> nanoparticles are well dispersed throughout carbon nanowalls template.
- Carbon nanowalls improve the capacitive behavior and rate capability of MnO<sub>2</sub>.
- The work conceptually provided a way in designing a 2D porous carbon nanowalls-based matrix for electroactive materials.

### ARTICLE INFO

#### Article history:

Received 14 July 2013

Received in revised form

19 September 2013

Accepted 16 October 2013

Available online 1 November 2013

#### Keywords:

Electrodeposition

Microwave plasma enhanced chemical

vapor deposition

Manganese dioxide

Carbon nanowalls

### ABSTRACT

Amorphous MnO<sub>2</sub>/carbon nanowalls composite films are developed for the supercapacitor applications. Synthesis of carbon nanowalls template is performed by plasma-enhanced chemical vapor deposition in a CO/H<sub>2</sub> microwave discharge system. A well dispersion of amorphous MnO<sub>2</sub> domains throughout carbon nanowalls template is obtained by potentiostatic anodic deposition technique. Carbon nanowalls enable to improve the capacitive behavior and rate capability of MnO<sub>2</sub>, a specific capacitance of 851 F g<sup>-1</sup> at a current density of 1 mA cm<sup>-2</sup> and charge transfer resistance of 1.02 Ω are obtained. MnO<sub>2</sub>/carbon nanowalls composite film exhibits energy density of 118 wh kg<sup>-1</sup>, power density of 783 wh kg<sup>-1</sup>, and capacitance retention of 92% after long cycle life of 2000 cycles by charging and discharging at 3 mA cm<sup>-2</sup>. The high density of atomic scale graphitic edges and large surface area of carbon nanowalls in conjunction with the presence of amorphous MnO<sub>2</sub> domains facilitate rapid electron and ion transport and hence offering the potential of the improved capacitive behavior.

© 2013 Elsevier B.V. All rights reserved.

### 1. Introduction

A sustainable energy supply is one of the most important scientific and technological challenges in the 21st century. Achieving this challenge will require not only increased energy efficiency but also new energy storage technologies to replace the rapid depleted fossil fuels. The increasing environmental pollution caused by consumption of fossil energy is considered as the foremost challenges that face mankind in present days, so a renewable and clean energy supply that can support the sustainable development of the global economy and society becomes more required than before.

Electrical energy that is generated by solar, wind, bio-mass, geothermal and other renewable forms offer many advantages over fossil fuel based sources. In order to maximize usage of these renewable sources, High performance electrochemical energy storage systems which are long lasting and clean that can match the production of renewable energy, in addition to match the fast development of portable electronics and hybrid electric vehicles with low CO<sub>2</sub> emissions, are needed as effective ways for solving fossil fuel depletion problems. Energy storage is usually required as an intermediate step to the versatile, clean, and efficient use of energy.

Supercapacitors, as one of the electrochemical energy storage systems, have acquired increasing importance due to their high power density [1–4]. However, supercapacitors often have low energy storage media due to the low specific capacitance of the currently available electrode materials. For this reason, the selection of a suitable electrode material is one of the keys to obtain good performance supercapacitors [3].

\* Corresponding author. Tel.: +20 1281229082; fax: +20 3 4599802.

E-mail addresses: [oneim99@yahoo.com](mailto:oneim99@yahoo.com), [ahmed.abdelmoneim@ejust.edu.eg](mailto:ahmed.abdelmoneim@ejust.edu.eg) (A. El-Moneim).

<sup>1</sup> On leave from Physical Chemistry Department, National Research Centre, Cairo, Egypt.

So far, manganese oxides have attracted significant interest as active electrode materials for electrochemical processes, particularly electrochemical capacitors (ECs) [5–19]. These oxides are characterized by reasonable specific capacitance, low-cost, abundance and environmentally friendly nature.

In general, hydrated manganese oxides exhibit specific capacitances within the 100–200 F g<sup>−1</sup> range in aqueous solutions. Poor electrical conductivity ( $\sim 10^5 \Omega \text{ cm}$ ) has been reported for micrometer-thick birnessite-type MnO<sub>2</sub> [18,20]. The specific capacitance and power characteristics of MnO<sub>2</sub> electrodes are ultimately limited by the high charge-transfer resistance. In addition to their poor electrical conductivity, another important issue is the electrochemical cyclability of MnO<sub>2</sub> electrodes. Active material dissolution during electrochemical cycling has been well recognized in some investigations, which accounts for the major capacitance loss of the MnO<sub>2</sub> electrodes. Mechanical issues, such as low structural stability and flexibility, also exist in MnO<sub>2</sub> electrodes resulting in degraded long-term electrochemical cycle life [20].

An important consideration for alleviating the poor electronic conductivity, chemical and mechanical stabilities, and flexibility of MnO<sub>2</sub> electrodes is to tailor the electrode architecture via applying an ultrathin layer of MnO<sub>2</sub> on the surface of a porous, high surface area and electronically conducting structure to shorten the solid state transport for ions and diffusion path lengths of electrons. This can produce a good electrochemical performance without sacrificing the mass-loading of the MnO<sub>2</sub> phase. The porous architectures can be carbon nanofoams, template mesoporous carbon, carbon nanowires, nanotube assemblies, chitosan and conductive polymers [7,20–23].

Meanwhile, novel nanostructured carbon materials, Carbon Nanowalls (CNWs) films, have attracted increasing attention in recent years. They can be described as two-dimensional (2D), several tens of nanometers in width, carbon nanostructures composed of self-aligned graphene nanodomains arranged vertically on a substrate [24]. Their high surface-to-volume ratio, high mechanical and chemical stability, high electrical conductivity, and the large amount of graphitic edge planes with a high surface activity have led to these materials being used in several applications such as catalyst supports, hydrogen adsorption and biological sensors [25–27]. Moreover, unlike other CVD-grown materials such as carbon nanotubes, these CNWs can be synthesized without a catalyst, which makes them especially attractive for investigating basic electrochemical phenomena [28].

To our knowledge, despite the increasing interest in CNWs as porous architectures for electrochemical applications as lithium-ion batteries and fuel cells, the use of these materials for supercapacitor applications has still not been reported. Thus, a deposition of thin film of nanostructured MnO<sub>2</sub> on CNWs is thought as an ideal approach to enhance the capacitive behavior of MnO<sub>2</sub> film for supercapacitor applications.

## 2. Experimental

### 2.1. Growth of CNWs

The production of CNW was carried out in a microwave plasma-enhanced chemical vapor deposition (MPECVD) with CO/H<sub>2</sub> microwave discharge system as shown in Fig. 1.

The MPECVD system used in this study is a modified ASTeX DPA25 plasma applicator in which the quartz discharge tube of 15 mm inner diameter is utilized. Nickel foam with an apparent area of 1 cm<sup>2</sup> was used as a substrate. The applied parameters of the CNWs deposition process were as follows: total flow rate, 50 sccm; CO flow rate, 46 sccm; H<sub>2</sub> flow rate, 4 sccm; total pressure, 250 Pa; microwave power, 80 W; deposition time, 18 s; substrate temperature, 700 °C.

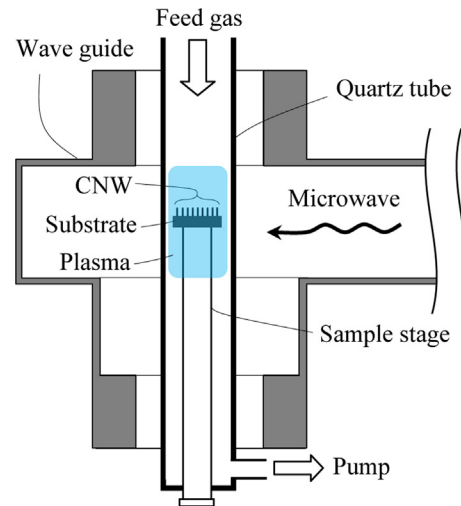


**Fig. 1.** Schematic diagram of microwave plasma-enhanced chemical vapor deposition (MPECVD) with CO/H<sub>2</sub> microwave discharge system for CNW deposition.

### 2.2. Electrochemical deposition of MnO<sub>2</sub>

The electrochemical anodic deposition of MnO<sub>2</sub> was carried out in 0.25 M (CH<sub>3</sub>COO)<sub>2</sub>Mn·4H<sub>2</sub>O electrolyte at 1 V(Ag/AgCl (KCl saturated)) using Pt-rod as a counter electrode and CNWs/Ni foam substrate as a working electrode. The mass of the deposited films was controlled by adjusting the total charge passed through the electrode during deposition process. The estimated mass loading of the deposited MnO<sub>2</sub> film was about 0.1 mg cm<sup>−2</sup>.

### 2.3. Structure and electrochemical characterizations of MnO<sub>2</sub>/CNW electrodes

The deposited films were observed using scanning electron microscope (Hitachi S-4500) and transmission electron microscopy (JEOL JEM-2010F). NRS-2100 Raman spectrometer with 514.5 nm wavelength incident laser light was used to analyze the carbon deposits of the films.

The electrochemical properties of the obtained films have been conducted using a three-electrode system in 0.5 M Na<sub>2</sub>SO<sub>4</sub> electrolyte. The cyclic voltammetry (CV), galvanostatic charge–discharge, and electrochemical impedance spectroscopy (EIS) studies have been performed using VersaSTAT3 potentiostat/galvanostat electrochemical system.

The CV behaviors were carried out within a potential range of 0–0.9 V vs. Ag/AgCl (KCl saturated) at scan rates of 10–300 mV s<sup>−1</sup>. Galvanostatic charge/discharge cycling was conducted at constant current densities of 1.0–10 mA cm<sup>−2</sup> between 0 and 1.0 V. The calculation methods of cyclic voltammetry specific capacitance (SC) and chronopotentiometry discharge SC values are given in detail elsewhere [18,19]. The SC was estimated according to the mass of MnO<sub>2</sub> film. The cycle life test was performed at current density 3 mA cm<sup>−2</sup> for 2000 cycles. The applied alternating current amplitude for impedance measurements was 10 mV root mean square in a frequency range of 0.1 Hz–7 kHz.

## 3. Results and discussion

### 3.1. Structure morphology of MnO<sub>2</sub>-free CNW film

Fig. 2(a–c) shows typical SEM images of CNW film at different magnifications. The images indicate the vertical growth of the two-dimensional carbon sheets with honeycomb structure on the Ni

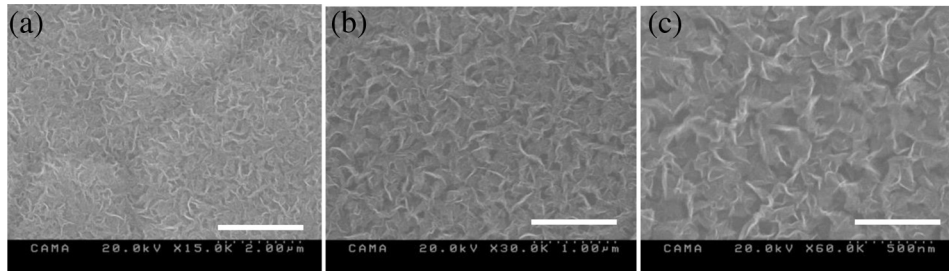


**Fig. 2.** Typical SEM images for CNW film, grown by MPECVD using CO/H<sub>2</sub> microwave discharge system for 18 s, at low (a), intermediate (b) and high (c) resolutions.

substrate. In addition to the vertically standing maze-like structure, isolated very thin nanosheets, less aligned petal-like, highly branched type, and a kind of porous film have been fabricated so far.

**Fig. 3(a–c)** depicts HRTEM images of MnO<sub>2</sub>-free CNW film at different magnifications. In general, the images confirm the 2D-configuration of the nanowalls, which exhibit both crumpled and folded areas. The individual walls have rather wavy structures. The growth direction of the walls are oriented perpendicularly to the nickel substrate, thereby favoring electrical conduction from the substrate and resulting in a large amount of exposed reactive edge planes [29]. The lattice structure of the crystallized carbon layers is clearly seen in the high-magnification HRTEM images in **Fig. 3(b)** and (c). As seen, the distance between the lattice fringes is about 0.34 nm, which corresponds to the reported one for CNW and that of graphite (002) planes of graphite structures [30,31].

**Fig. 4** illustrates Raman spectrum of the carbon deposits in the MnO<sub>2</sub>/CNW film. In this spectrum, two main bands of carbon material are obtained, a D-band at 1360 cm<sup>-1</sup>, a G-band at 1590 cm<sup>-1</sup>. The detected D-band is attributed to defects due to the finite crystallite size or edges of graphene layers; while the G-band represents the in-plane bond-stretching motion of the pairs of carbon sp<sup>2</sup> atoms which indicates the presence of crystalline graphene layers. In addition, a small peak is observed at about 1620 cm<sup>-1</sup>. This band corresponds to D'-band, which emerges with the D-band indicating the disorder and associated with finite-size graphite crystals and graphene edges. The D'-band appears in the graphite-like carbons with relatively low disorder such as microcrystalline graphite and glassy carbon, while it can't be observed in

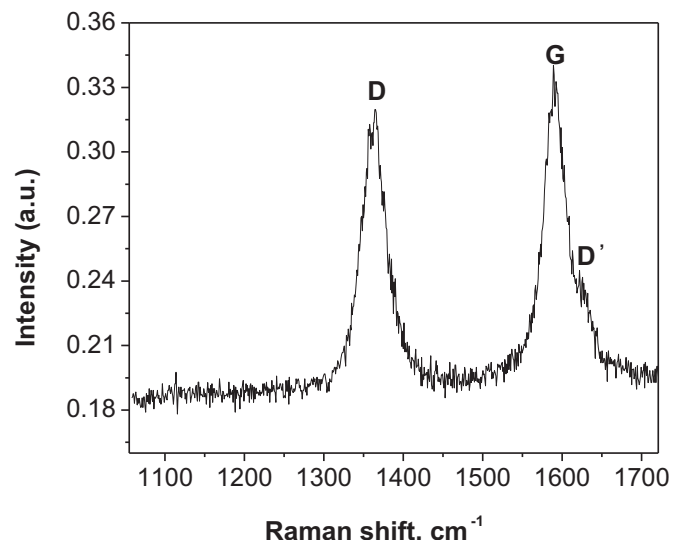


**Fig. 4.** Raman spectrum of the carbon deposits in the MnO<sub>2</sub>/CNW film measured using the 514.5 nm line of an Ar laser.

significantly disordered carbons such as carbon black. The strong D-band peak and D'-band peak suggest a more nanocrystalline structure and presence of graphene edges and defects such as distortion, vacancies and straining to graphitic lattices, which are prevalent features of CNWs [32].

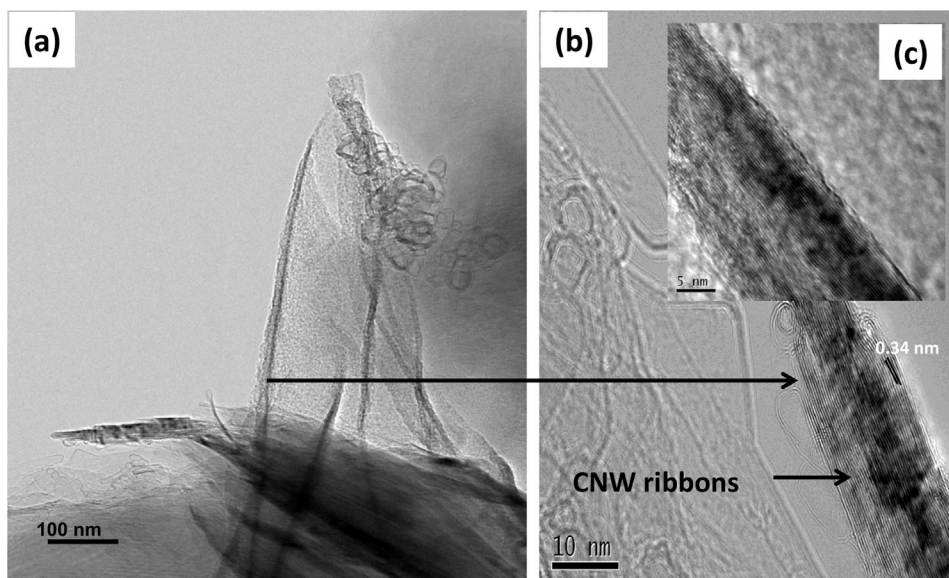


**Fig. 3.** Typical TEM images of CNW film, grown by MPECVD using CO/H<sub>2</sub> microwave discharge system for 18 s, at low (a) and high (b) and (c) resolutions.

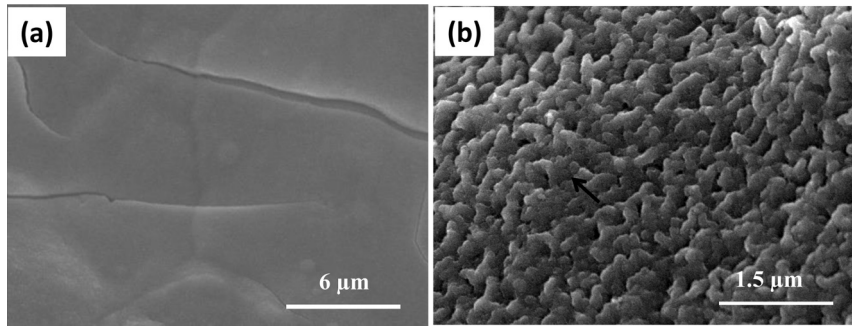


Fig. 5. SEM images of CNW-free  $\text{MnO}_2$  (a) and  $\text{MnO}_2/\text{CNW}$  (b) films.

### 3.2. Morphology of $\text{MnO}_2/\text{CNW}$ film

Fig. 5 shows the SEM images of CNW-free  $\text{MnO}_2$  film (a) and the  $\text{MnO}_2/\text{CNW}$  film (b). In comparison, the image of CNW-free  $\text{MnO}_2$  film (a) shows smooth surface with continuous cracks due to drying shrinkage, while the image of  $\text{MnO}_2/\text{CNW}$  film (b) exhibits crack-free surface and the morphology of the deposited  $\text{MnO}_2$  follows the structure texture of the underlying CNW film.

Fig. 6 depicts HRTEM images for CNW-free  $\text{MnO}_2$  (a) and the  $\text{MnO}_2/\text{CNW}$  (b) films. As can be seen, the  $\text{MnO}_2$  polymorph birnessite is clearly visible in the image of CNW-free  $\text{MnO}_2$  film (a), and tends to disappear with the deposition on CNW template (b). This indicates that CNW template enables the deposition of amorphous  $\text{MnO}_2$  film. In fact, the formation of amorphous phase-based materials is generally feasible for supercapacitor and sensing applications due to the large accessible surface area and easy penetration of ions through the bulk of active materials. Meanwhile, the image of  $\text{MnO}_2/\text{CNW}$  film (b) clearly shows the unique nanostructure of the CNW template is still maintained, even after the deposition of  $\text{MnO}_2$  film. In addition, the  $\text{MnO}_2$  amorphous-domains, large dark spots, are dispersible throughout exposed reactive edge planes of CNWs and dictate the interlayer spacing between the stand free graphene sheets. Hence, the development of nanocomposite material with such high surface to volume ratio would be expected to retain electronic conductivity, electrochemical stability and mechanical strength upon cycling, thus providing an opportunity to tune the material for optimal capacitive performance.

### 3.3. Electrochemical supercapacitive behavior

#### 3.3.1. Cyclic voltammetry

Fig. 7 indicates the CV comparison curves for CNW-free  $\text{MnO}_2$  (a) and the  $\text{MnO}_2/\text{CNW}$  (b) films measured in 0.5 M  $\text{Na}_2\text{SO}_4$  electrolyte at a scan rate of  $90 \text{ mV s}^{-1}$ . The CV curve for  $\text{MnO}_2$ -free CNW film is also given for comparison. The inset of Fig. 7 presents the variation in the voltammetry SC with the scan rate for the  $\text{MnO}_2$ -based films.

It is shown that the CV curves of CNW-free  $\text{MnO}_2$  (b) and  $\text{MnO}_2/\text{CNW}$  (c) films show nearly rectangular shape and characteristic mirror-image without clear redox peaks in the potential range 0–0.9 V, indicative of highly capacitive behavior with good ion response. The capacitive contribution of  $\text{MnO}_2$ -free CNW film (a) is negligible compared with CNW-free  $\text{MnO}_2$  (b) and  $\text{MnO}_2/\text{CNW}$  (c) films. The highest SC values, obtained at a scan rate  $10 \text{ mV s}^{-1}$ , for CNW-free  $\text{MnO}_2$  and  $\text{MnO}_2/\text{CNW}$  films are 488 and  $685 \text{ F g}^{-1}$ , respectively. This means that CNWs provide more active sites for an efficient utilization of  $\text{MnO}_2$  as promising pseudo-capacitance material.

As seen in the inset of Fig. 7, a clear gradual decrease in the specific capacitance is noticed with the increase in the scan rate indicating the high porous nature of the deposited films. Meanwhile, the decrease in specific capacitance for  $\text{MnO}_2/\text{CNW}$  film with the scan rate is found to be lower than that of CNW-free  $\text{MnO}_2$  film, indicating the stability inducing effect of CNWs.

#### 3.3.2. Galvanostatic charge–discharge characteristic

To further clarify the effect of CNWs on the capacitive behavior and rate capability of  $\text{MnO}_2$  film, the charge and discharge behavior was examined by chronopotentiometry.

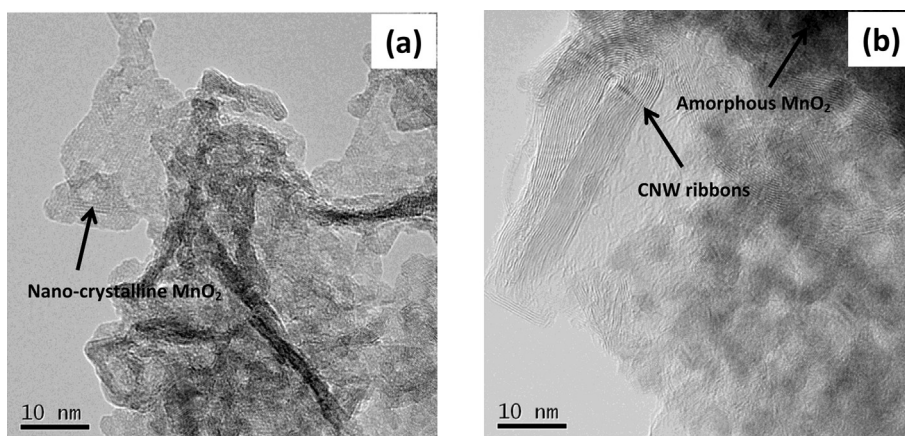
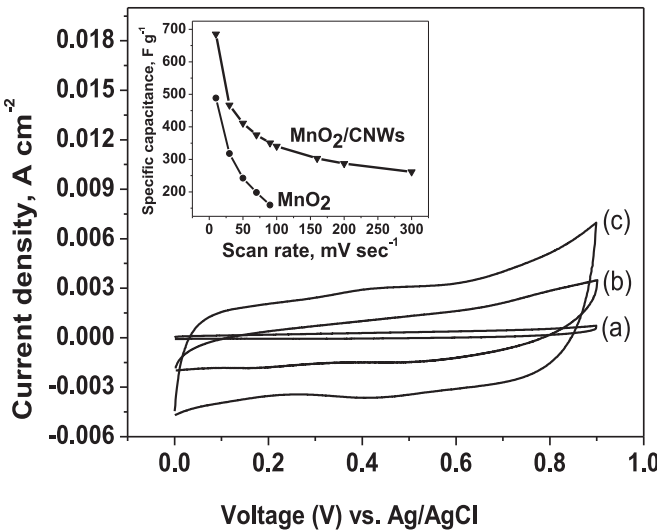


Fig. 6. High-resolution TEM images of CNW-free  $\text{MnO}_2$  (a) and  $\text{MnO}_2/\text{CNW}$  (b) films.



**Fig. 7.** CV curves for MnO<sub>2</sub>-free CNW (a), CNW-free MnO<sub>2</sub> (b), and MnO<sub>2</sub>/CNW (c) films measured in 0.5 M Na<sub>2</sub>SO<sub>4</sub> electrolyte at a scan rate of 90 mV s<sup>-1</sup> and 30 °C. The inset presents the variation of specific capacitance for MnO<sub>2</sub>-based films with scan rate.

**Fig. 8** shows charge–discharge profiles of MnO<sub>2</sub>-free CNW (a), CNW-free MnO<sub>2</sub> (b), and MnO<sub>2</sub>/CNW (c) films measured in 0.5 M Na<sub>2</sub>SO<sub>4</sub> electrolyte at 30 °C at current density of 1.0 mA cm<sup>-2</sup>. The inset presents the variation of the discharge SC for the examined films with the current density.

In principle, the discharge profile of any oxide film with capacitive characteristics is basically consisted of three parts: a resistive component from sudden voltage drop (IR drop) due to the internal resistance of the deposited film, the capacitance component related to the voltage change due to ion separation in the double layer region at the electrode interface, and finally faradaic component in the longer time region due to charge transfer reaction of the film.

As can be seen in **Fig. 8**, the IR drop for MnO<sub>2</sub>/CNW film (c) is less than that of CNW-free MnO<sub>2</sub> (b) and MnO<sub>2</sub>-free CNW (a) films, indicating that the MnO<sub>2</sub>/CNW film (c) have the lower internal

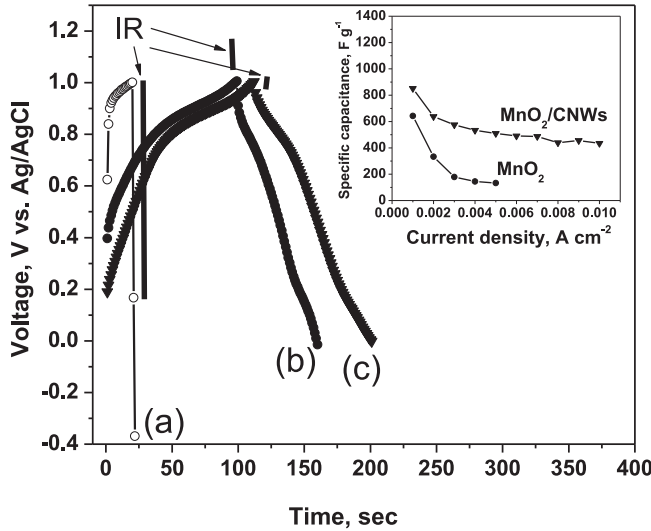


**Fig. 8.** Galvanostatic charge–discharge curves of MnO<sub>2</sub>-free CNW (a), CNW-free MnO<sub>2</sub> (b), and MnO<sub>2</sub>/CNW (c) films measured in 0.5 M Na<sub>2</sub>SO<sub>4</sub> electrolyte at a current density of 1 mA cm<sup>-2</sup> and 30 °C. The inset presents the variation of the discharge SC of the deposited films with the applied current density.

resistance, ultimately lower charge transfer resistance, than CNW-free MnO<sub>2</sub> films. Moreover, the MnO<sub>2</sub>/CNW film (c) show longer discharge time, which is equivalent to higher specific capacitance, than CNW-free MnO<sub>2</sub> (b). Meanwhile, the inset of **Fig. 8**, clearly shows that the discharge SC gradually decreases by applying high current density, and the highest SC values for CNW-free MnO<sub>2</sub> and MnO<sub>2</sub>/CNW films are 643 and 851  $\text{F g}^{-1}$ , respectively. This indicates that MnO<sub>2</sub>/CNW nanocomposite film does not only show higher SC but also better capability rate of charge–discharge than CNW-free MnO<sub>2</sub> film. This is in coincidence in the CV results presented in **Fig. 7**.

In brief, the MnO<sub>2</sub>/CNW nanocomposite films are indeed promising architectures, which are able to improve the electrochemical performance of MnO<sub>2</sub> pseudo-capacitance material.

In order to understand the reason behind the unique performance of the MnO<sub>2</sub>/CNW nanocomposite electrode compared to CNW-free MnO<sub>2</sub> electrode, comparative electrochemical impedance spectroscopy (EIS) data were collected.

### 3.3.3. Electrochemical impedance spectroscopy studies

**Fig. 9** shows Nyquist plots for CNWs-free MnO<sub>2</sub> (a) and MnO<sub>2</sub>/CNW (b) films measured in 0.5 M Na<sub>2</sub>SO<sub>4</sub> electrolyte at 30 °C. The inset represents the high frequency region of **Fig. 9**.

In general, the impedance spectra of films used in supercapacitor application are composed of a high-frequency arc region followed by a low-frequency line. The very high-frequency intercept at the real impedance part ( $Z'$ ) at the beginning of the arc represents the equivalent series resistance (ESR), which includes the ionic resistance of the electrolyte, the intrinsic resistance of the active material, intrinsic resistance of current collector, and the contact resistance at the interface between active material and current collector. The power density of supercapacitors depends strongly on the ESR. The arc in the high-frequency region corresponds to the charge transfer resistance ( $R_{ct}$ ) caused by the charge transfer process (Faradaic reactions) and double layer charging on the electrode surface. The magnitude of the  $R_{ct}$  can typically be derived from diameter of the arc. The line at lower frequency region is a result of ion diffusion/transport (Warburg resistance) through the pores of the deposited films [33–36].

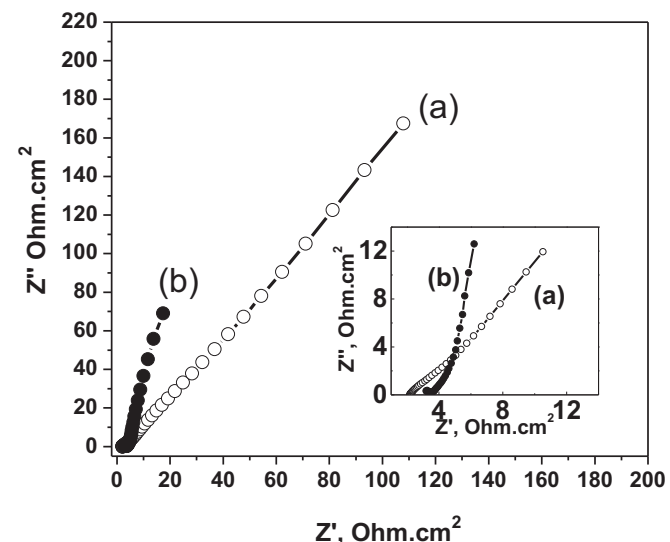


**Fig. 9.** Nyquist plots of CNW-free MnO<sub>2</sub> (a) and MnO<sub>2</sub>/CNW (b) films measured in 0.5 M Na<sub>2</sub>SO<sub>4</sub> electrolyte in the frequency range of 0.1 Hz–7 kHz at 10 mV amplitude at 30 °C. The inset represents the high frequency region of the recorded full impedance plots of CNW-free MnO<sub>2</sub> (a) and MnO<sub>2</sub>/CNW (b) films.

The fitting of Nyquist plots presented in Fig. 9 revealed that the estimated ESR values for CNW-free  $\text{MnO}_2$  (a) and  $\text{MnO}_2/\text{CNW}$  (b) films are 2.04 and 3.19  $\Omega$ , respectively. The results indicate that the contact resistance affects ESR with presence of CNWs template as compared with its absence. On the other hand, the estimated  $R_{ct}$  values for CNW-free  $\text{MnO}_2$  (a) and  $\text{MnO}_2/\text{CNW}$  (b) films are 3.28 and 1.02  $\Omega$ , respectively. The decrease in the  $R_{ct}$  value with presence of CNW template reflects the enhancement in the electronic and ionic conductivities of the amorphous  $\text{MnO}_2$  domains.

Meanwhile, the slope of the Nyquist plot in the low frequency region for  $\text{MnO}_2/\text{CNW}$  film is larger than, i.e. the decreasing in Warburg resistance (or diffusion resistance), that of CNW-free  $\text{MnO}_2$  film. Such decrease in diffusion resistance is likely a result of the amorphous nature of the  $\text{MnO}_2$  and the presence of inter-layer spacing among stand-free CNW sheets, thus decreasing the overall kinetic barriers to the diffusion of ions into the  $\text{MnO}_2/\text{CNW}$  nanostructure.

### 3.3.4. Galvanostatic charge–discharge cyclic stability

Fig. 10 presents the electrochemical stability of CNW-free  $\text{MnO}_2$  (a) and  $\text{MnO}_2/\text{CNW}$  (b) films investigated in 0.5 M  $\text{Na}_2\text{SO}_4$  electrolyte at 30 °C by charging and discharging at 3  $\text{mA cm}^{-2}$  for 2000 cycles. Noticeable specific capacitance loss is observed for CNW-free  $\text{MnO}_2$  film (a). The CNW-free  $\text{MnO}_2$  film only retained 56% of its initial capacitance after 300 cycles, while  $\text{MnO}_2/\text{CNW}$  film (b) showed a little decrease in the value of specific capacitance (down to 85% of its initial value) during the 100 cycles and then the specific capacitance increased again up to 92% of its initial value after 2000 cycles, indicating electro-activation as well as long term electrochemical and mechanical cycling stabilities.

In brief, we have successfully deposited amorphous  $\text{MnO}_2$  on CNW template through two processes: using PECVD system that offer a more feasible process for the fabrication of CNWs in a very short time, and a simple and appropriate synthesis process (electrodeposition), to prepare a composite electrode with hierarchical porous structure and superior capacitive behavior and capability rate.  $\text{MnO}_2/\text{CNW}$  nanocomposite electrode exhibited energy density of 118  $\text{wh kg}^{-1}$ , power density of 783  $\text{wh kg}^{-1}$  and high capacitance retention of 92% after long cycle life of 2000 cycles by charging and discharging at 3  $\text{mA cm}^{-2}$ . As a consequence,  $\text{MnO}_2/\text{CNW}$  nanocomposite electrode can be presented a new promising

electrode for electrochemical supercapacitors application. Most importantly, this work conceptually provides a way in designing a 2D porous CNW-based matrix for many electroactive materials.

## 4. Conclusions

Using a modified ASTeX DPA25 plasma applicator experimental design, CNW deposit has been obtained. Amorphous  $\text{MnO}_2$  thin film was successfully deposited onto CNW deposits by potentiostatic anodic deposition method on nickel foam current collectors from  $(\text{CH}_3\text{COO})_2\text{Mn} \cdot 4\text{H}_2\text{O}$  solution. It has been shown that  $\text{MnO}_2/\text{CNW}$  nanocomposite electrode provides promising capacitive performance. A specific capacitance of 851  $\text{F g}^{-1}$  at current density 1  $\text{mA cm}^{-2}$  was obtained for the  $\text{MnO}_2/\text{CNW}$  nanocomposite electrode in 0.5 M  $\text{Na}_2\text{SO}_4$  electrolyte. The specific capacitance of the electrode has a good stability during 2000 cycles at a current density of 3  $\text{mA cm}^{-2}$ . The excellent capacitive behavior shows that the amorphous  $\text{MnO}_2$  films with CNWs template can be considered as a promising electrode material for high performance supercapacitors. Finally, this work conceptually provides a way in designing a 2D porous CNW-based matrix for many electroactive materials.

## Acknowledgments

The authors gratefully acknowledge the Missions Sector-Higher Education Ministry, Egypt for financial support through this work, and Materials Science and Engineering Department at E-JUST. We thank Mr. K. Hori and J. Koki of the Center for Advanced Material Analysis in Tokyo Tech. for assistance with the TEM observations.

## References

- [1] Q. Cheng, J. Tang, J. Ma, H. Zhang, N. Shinya, L.-C. Qin, Carbon 49 (2011) 2917–2925.
- [2] B.E. Conway, Electrochemical Supercapacitors: Scientific Fundamentals and Technological Applications, Plenum Press, New York [u.a.], 1999.
- [3] A.F. Burke, T.C. Murphy, D.H. Gough, B. Vyas, T. Takamura, J.R. H (Eds.), Materials Research Society, 1995. Pittsburgh, PA.
- [4] L.T. Lam, R. Louey, J. Power Sources 158 (2006) 1140–1148.
- [5] N.-L. Wu, Mater. Chem. Phys. 75 (2002) 6–11.
- [6] T. Brousse, D. Bélanger, Electrochim. Solid-State Lett. 6 (2003) A244–A248.
- [7] T. Brousse, M. Toupin, D. Bélanger, J. Electrochim. Soc. 151 (2004) A614–A622.
- [8] H.Y. Lee, J.B. Goodenough, J. Solid State Chem. 144 (1999) 220–223.
- [9] H.Y. Lee, V. Manivannan, J.B. Goodenough, Comp. Rend. l'Acad Sci. – Ser. IIC – Chem. 2 (1999) 565–577.
- [10] M. Toupin, T. Brousse, D. Belanger, Chem. Mater. A Publ. Am. Chem. Soc. 16 (2004) 3184–3190.
- [11] C.Y. Lee, H.M. Tsai, H.J. Chuang, S.Y. Li, P. Lin, T.Y. Tseng, J. Electrochim. Soc. 152 (2005) A716–A720.
- [12] A.A. El-Moneim, B.M. Baker, Int. J. Electrochim. Sci. 7 (2012) 671–685.
- [13] A.A. El-Moneim, Int. J. Hydrogen Energy 36 (2011) 13398–13406.
- [14] A.A. El-Moneim, J. Bhattacharai, Z. Kato, K. Izumiya, N. Kumagai, K. Hashimoto, ECS Trans. 25 (2010) 127–137.
- [15] A.A. El-Moneim, K. Kumagai, K. Hashimoto, Mater. Trans. 66 (2009) 1969–1977.
- [16] A.A. El-Moneim, N. Kumagai, K. Asami, K. Hashimoto, Mater. Trans. 46 (2005) 309–316.
- [17] K. Hashimoto, H. Shinomiya, A. Nakazawa, Z. Kato, A.A. El-Moneim, Y. Niizeki, K. Asami, ECS Trans. 1 (2006) 49–59.
- [18] S. Hassan, M. Suzuki, A. Abd El-Moneim, EEE Electr. Electron. Eng. 2 (2012) 18–22.
- [19] S. Hassan, M. Suzuki, A. Abd El-Moneim, Am. J. Mater. Sci. 2 (2012) 11–14.
- [20] W. Wei, X. Cui, W. Chen, D.G. Ivey, Chem. Soc. Rev. 40 (2011) 1697–1721.
- [21] H. Jiang, L. Yang, C. Li, C. Yan, P.S. Lee, J. Ma, Energy Environ. Sci. 4 (2011) 1813–1819.
- [22] H. Jiang, J. Ma, C. Li, Adv. Mater. 24 (2012) 4197–4202.
- [23] S. Hassan, M. Suzuki, A.A. El-Moneim, J. Power Sources 246 (2014) 68–73.
- [24] M. Hiramatsu, M. Hori, Carbon Nanowalls: Synthesis and Emerging Applications, Springer, Wien; New York, 2010.
- [25] Y. Wu, P. Qiao, T. Chong, Z. Shen, Adv. Mater. 14 (2002) 64–67.
- [26] K. Shiji, M. Hiramatsu, A. Enomoto, M. Nakamura, H. Amano, M. Hori, Diam. Relat. Mater. 14 (2005) 831–834.

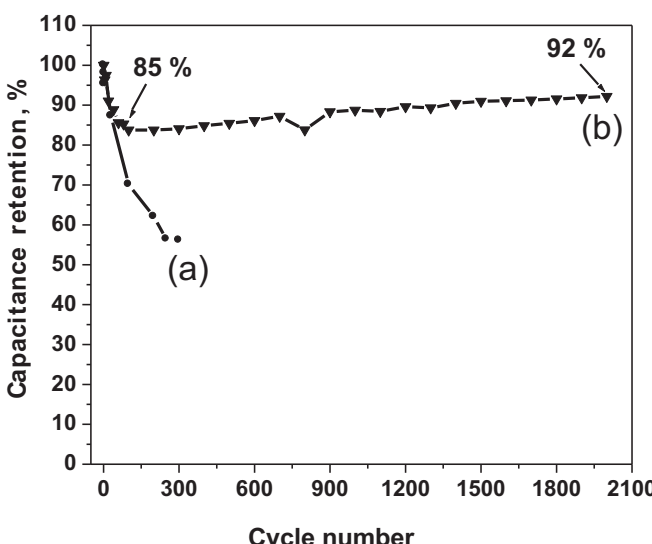


Fig. 10. Life-cycle data of CNW-free  $\text{MnO}_2$  (a) and  $\text{MnO}_2/\text{CNW}$  (b) films investigated in 0.5 M  $\text{Na}_2\text{SO}_4$  electrolyte at 30 °C at current density 3  $\text{mA cm}^{-2}$ .

- [27] Y. Wu, B. Yang, B. Zong, H. Sun, Z. Shen, Y. Feng, *J. Mater. Chem.* 14 (2004) 469–477.
- [28] O. Tanaike, N. Kitada, H. Yoshimura, H. Hatori, K. Kojima, M. Tachibana, *Solid State Ionics* 180 (2009) 381–385.
- [29] Z. González, S. Vizireanu, G. Dinescu, C. Blanco, R. Santamaría, *Nano Energy* 1 (2012) 833–839.
- [30] K. Tanaka, M. Yoshimura, A. Okamoto, K. Ueda, *Jpn. J. Appl. Phys.* 44 (2005) 2074–2076.
- [31] K. Kobayashi, M. Tanimura, H. Nakai, A. Yoshimura, H. Yoshimura, K. Kojima, M. Tachibana, *J. Appl. Phys.* 101 (2007) 94306.
- [32] S. Mori, T. Ueno, M. Suzuki, *Diam. Relat. Mater.* 20 (2011) 1129–1132.
- [33] Q. Lu, Y. Zhou, *J. Power Sources* 196 (2011) 4088–4094.
- [34] A. Celzard, F. Collas, J.F. Maréché, G. Furdin, I. Rey, *J. Power Sources* 108 (2002) 153–162.
- [35] T. Tüken, B. Yazıcı, M. Erbil, *Prog. Org. Coat.* 50 (2004) 115–122.
- [36] M.D. Stoller, S. Park, Y. Zhu, J. An, R.S. Ruoff, *Nano Lett.* 8 (2008) 3498–3502.